



**HAL**  
open science

## **UHBR Open-Test-Case Fan ECL5/CATANA**

Valdo Pagès, Pierre Duquesne, Stephane Aubert, Laurent Blanc, Pascal Ferrand, Xavier Ottavy, Christoph Brandstetter

► **To cite this version:**

Valdo Pagès, Pierre Duquesne, Stephane Aubert, Laurent Blanc, Pascal Ferrand, et al.. UHBR Open-Test-Case Fan ECL5/CATANA. *International Journal of Turbomachinery, Propulsion and Power*, 2022, 7 (2), 10.3390/ijtp7020017 . hal-03765815v1

**HAL Id: hal-03765815**

**<https://hal.science/hal-03765815v1>**

Submitted on 31 Aug 2022 (v1), last revised 14 Nov 2022 (v2)

**HAL** is a multi-disciplinary open access archive for the deposit and dissemination of scientific research documents, whether they are published or not. The documents may come from teaching and research institutions in France or abroad, or from public or private research centers.

L'archive ouverte pluridisciplinaire **HAL**, est destinée au dépôt et à la diffusion de documents scientifiques de niveau recherche, publiés ou non, émanant des établissements d'enseignement et de recherche français ou étrangers, des laboratoires publics ou privés.

# UHBR Open-Test-Case Fan ECL5/CATANA

Valdo Pagès <sup>1</sup>, Pierre Duquesne <sup>1</sup>, Stéphane Aubert <sup>1</sup>, Laurent Blanc <sup>2</sup>, Pascal Ferrand <sup>1</sup>, Xavier Ottavy <sup>1</sup>, Christoph Brandstetter <sup>1\*</sup>

<sup>1</sup> Univ. Lyon, Ecole Centrale de Lyon, CNRS, Univ. Claude Bernard Lyon 1, INSA Lyon, LMFA, UMR5509, 69130, Ecully, France

<sup>2</sup> Univ. Lyon, Ecole Centrale de Lyon, CNRS, UMR5513, LTDS, 69130, Ecully, France

**Abstract:** Application of composite fans enables disruptive design possibilities but increases sensitivity to multi-physical resonance between aerodynamic, structure dynamic and acoustic phenomena. As a result, aeroelastic problems increasingly set the stability limit. Test cases of representative geometries without industrial restrictions are a key element of an open scientific culture but currently non-existent in the turbomachinery community. In order to provide a multi-physical validation benchmark representative of near future UHBR fan concepts, the open test case fan stage ECL5 has been developed at Ecole Centrale de Lyon. Design intention was to develop a geometry with high efficiency and a wide stability range that can be realized using carbon fibre composites. This publication aims to introduce the final test case which is currently fabricated and will be experimentally tested. The fan blades are composed of a laminate made of unidirectional carbon fibres and epoxy composite plies. Their structural properties and the ply orientations are presented. To characterise the test case, details are given on aerodynamic design of the whole stage, structure dynamics of the fan and aeroelastic stability of the fan. These are obtained with a state-of-art industrial design process: static and modal FEM, RANS and LRANS simulations. Aerodynamic analysis focuses on performance and shows critical flow structures like tip leakage flow, radial flow migration and flow separations. Mechanical modes of the fan are described and discussed in the context of aeroelastic interactions. Their frequency distribution is validated in terms of resonance risk with respect to synchronous vibration. Aeroelastic stability of the fan is evaluated at representative operating points with a systematic approach. Potential instabilities are observed far from the operating line, not compromising experimental campaigns.

**Keywords:** Fan; Composite; Aeroelasticity; Flutter; Aeroacoustics

**Citation:** Pagès V.; Duquesne P.; Aubert S.; Blanc L.; Ferrand P.; Ottavy X.; Brandstetter C. UHBR Open-Test-Case Fan ECL5/CATANA. *Journal Not Specified* **2021**, *1*, 0. <https://doi.org/>

Received:  
Accepted:  
Published:

**Publisher's Note:** MDPI stays neutral with regard to jurisdictional claims in published maps and institutional affiliations.

**Copyright:** © 2022 by the author. Submitted to *Journal Not Specified* for possible open access publication under the terms and conditions of the Creative Commons Attribution (CC BY) license (<https://creativecommons.org/licenses/by/4.0/>).

## 1. Introduction

With application of modern lightweight blade geometries, aeroelastic coupling phenomena tend to reduce the operating range of compressors and fans in aircraft propulsion engines. As synchronous excitation mechanisms are well understood today, the most challenging aeroelastic phenomena for future turbomachinery applications are of non-synchronous<sup>1</sup> nature. A list of these phenomena is presented hereafter: **Flutter** is defined as self-excited blade vibration and usually involves blade-to-blade coupling. It is considered as initially small amplitude blade oscillation in a specific eigenmode that exponentially amplifies through a positive feedback loop with the aerodynamic field (negative aerodynamic damping). Linear modelling approaches are capable to predict the onset of this mechanism and to determine critical modes and to develop countermeasures. The disturbance is only dependent on the blade vibration and disappears as soon as the vibration stops. For large vibration amplitudes limit-cycle-oscillation may occur due to aerodynamic or structure dynamic non-linearity. For

<sup>1</sup> not a multiple of the shaft rotation speed

36 turbo-engine fans critical modes are typically dependent on swirling acoustic modes  
37 that develop between the inlet and the fan stage [1].

38 **Buffeting** describes the interaction between an aerodynamic instability (typically  
39 vortex shedding) that comprises a characteristic frequency and blade vibration in a spe-  
40 cific eigenmode. Typically, no circumferential blade-to-blade coupling is necessary but  
41 often planar acoustic duct modes establish and synchronize the phase of the aerodynamic  
42 instabilities leading to a zero-nodal-diameter vibration [2].

43 **Rotating stall** is a purely aerodynamic phenomenon occurring due to overloading  
44 of a blade row and subsequent flow separation leading to the establishment of circumfer-  
45 entially propagating stall-cells. It typically excites structural eigenmodes due to unsteady  
46 loading but for small amplitudes the propagation is not coupled with the blade vibration  
47 [3].

48 **Non-synchronous forced response:** in multistage compressors, a non-synchronous  
49 coupling mechanism between a trapped acoustic mode, coincident with a structural  
50 vibration pattern has been observed [4]. The phenomenon is less relevant for fan  
51 applications.

52 **Convective Non-Synchronous-Vibration (NSV):** Typically occurring close to the  
53 stability limit but before the onset of rotating stall, a complex lock-in mechanism between  
54 propagating aerodynamic vorticity disturbances and blade vibration is described under  
55 the term NSV [5,6]. Blade vibration leads to the change of free vorticity or even the  
56 formation of radial vortices in the passage flow which are convected from blade to blade  
57 if sufficient blockage is present in the passage. Interaction with trailing blades leads  
58 to modal forcing and the shedding of subsequent vorticity. Propagating aerodynamic  
59 disturbances can lock-in with structural vibration patterns and lead to a coherent fluid-  
60 structural interaction. The phenomenon needs to be differentiated from flutter as the  
61 aerodynamic disturbance appears without blade vibration and has a characteristic  
62 convective propagation speed (typically described under the term rotating-instability).

63 For all of the described phenomena, the flow structure in the tip region and particu-  
64 larly the influence of the tip leakage flow and the passage shock is of great importance.  
65 Significant blockage enables the circumferential transport of disturbances or provokes  
66 separation of the boundary layer which may be susceptible to acoustic or structure-  
67 dynamic feedback.

68 For high-speed fans rotating stall, buffeting and flutter are the most common  
69 instability mechanisms and are well understood today. The establishment of UHBR-  
70 configurations with low-speed fans however leads to a substantial change of relevant  
71 characteristics.

- 72 • Low-speed fans will predominantly operate on the flat part of the compression  
73 characteristic, making them more susceptible for stall-driven instability [7].
- 74 • The flutter frequencies (in the stationary frame) will be lower compared to high-  
75 speed designs. Acoustic liners in the intake, which are designed to attenuate higher  
76 frequency community noise will not affect the modes relevant for aero-elastic  
77 instability.
- 78 • The intake length will be shorter for low-speed fans, leading to stronger inflow  
79 asymmetry and altered acoustic interaction [8]. This gives rise to stronger broad-  
80 band excitation and shifted resonance frequencies.
- 81 • The relative Mach number and shock strength are lower, the tip-clearance relative  
82 to the blade chord and solidity<sup>2</sup> are smaller than for conventional direct-drive fans  
83 and more sensitive to geometric variability [9].
- 84 • A strongly nonlinear fluid-structure-interaction at low-frequencies has been ob-  
85 served for fans with low solidity related to the pressure untwist of the blades. At  
86 transonic conditions, slight deviations of the local stagger angle at the blade tip  
87 can cause a fundamentally different shock structure between adjacent blades that

---

<sup>2</sup> solidity = blade chord length / pitch

88 affects the stability of distinct rotor sections [10]. This circumstance affects the applicability of promising methods like intentional blade mistuning [11] to suppress the development of circumferentially propagating modes.

91 A selection of the state of the art High-Bypass-Ratio engines is presented in Figure 1<sup>3</sup>. The propulsion industry has focused on different strategies but all showing common goals: the reduction of tip speed, the reduction of number of blades and the reduction of individual blade weight. General Electric started in the 1990s with the establishment of layered carbon fibre composite fan blades in the GE90 engine for wide body aircrafts and is the only manufacturer with in-service composite fans. The more recent GENx shows a reduced blade number of 18. Following this development, the CFM LEAP engine has been established for the A320neo class, with 18 blades constructed from 3d-woven carbon fibres. Pratt&Whitney introduced the first Geared Turbofan with 20 (hybrid)-metallic blades, also for the A320neo class. Still following a conventional approach in fan design recent Rolls-Royce engines still comprise hollow titanium blades but technology demonstrators based on variants of the Trent1000 engine incorporate composite fibre fan blades. Exemplarily shown in Figure 1 is the fan of the Trent XWB engine for the Airbus A350 high bypass engine with 22 blades (Trent 7000 has 20 blades).



Figure 1. Selection of established modern (Ultra)-High-Bypass-Ratio Engines

105 All of the shown fan blades comprise significant 3D-features, particularly forward  
 106 sweep which is known to be beneficial for aerodynamic performance but emphasize  
 107 aeroelastic sensitivity for torsional or chordwise bending modes and particularly NSV.  
 108 Recent research [12,13] showed that the use of anisotropic properties of composite in  
 109 fans could help to improve both mechanics and aerodynamics. Composites also present  
 110 potential to control flutter by modification of eigenmodes [14].

111 In order to enable further technological advancements into this direction, extensive  
 112 research is necessary to identify and characterize the relevant instability mechanisms for  
 113 the novel type of low-speed fans. Particularly the complex flow structure at part load  
 114 and part speed is challenging for state-of-the-art numerical approaches and requires  
 115 experimental benchmark data on representative geometries.

116 To address these research objectives, an extensive research program in collaboration  
 117 between Ecole Centrale de Lyon and Von Karman Institute for Fluid Dynamics has  
 118 been initiated. A fan module, ECL5, fabricated from composite material has been  
 119 developed as an open test case. It will be investigated with a focus on non-synchronous  
 120 coupling mechanisms between aerodynamics, acoustics and structure dynamics within  
 121 the European CleanSky 2 project CATANA (Composite Aeroelastics and Aeroacoustics,  
 122 [catana.ec-lyon.fr](https://catana.ec-lyon.fr)). The fan stage has been designed at Ecole Centrale de Lyon with the

<sup>3</sup> image sources a) <https://www.geaviation.com/commercial/engines/ge90-engine>, b) <https://www.geaviation.com/commercial/engines/genx-engine> <https://c-fan.com/products/>, c) <https://www.cfmaeroengines.com/engines/leap/>, d) <https://www.flugrevue.de/flugzeugbau/getriebefan-triebwerke-pratt-whitney-will-probleme-beseitigen/>, e) <https://www.airlinerratings.com/news/a350s-trent-xwb-engine-hits-twin-milestones/>

123 intention to be representative of near-future composite low-speed fans in the following  
 124 terms:

- 125 1. General aerodynamic design parameters (Mach number, blade loading, solidity,  
 126 aspect ratio, hub-to-tip ratio, mass flow density, etc.)
- 127 2. Aerodynamic flow structure due to its influence on instability mechanisms (shock  
 128 patterns, radial flow migration, secondary flow, separations, etc.)

129 From the current point of view, the most promising research configuration is a  
 130 UHBR low-speed fan stage with high subsonic design speed, designated to be installed  
 131 in midrange jets (like Airbus A320neo). Hence, the open test case ECL5 that will be  
 132 introduced in the following has been developed from an extrapolation of industrial  
 133 concepts for current low-speed designs. In Figure 2<sup>4</sup>, the final design is shown in  
 134 comparison to the recently certified GE9x and the Rolls Royce UltraFan technology  
 135 demonstrator.



Figure 2. Modern industrial low-speed composite fans and Open-Test-Case ECL5/CATANA (CAD)

136 In the following, the final design and the composite structure of the fan are pre-  
 137 sented. Details are given on the modelling strategies used to simulate the different  
 138 physics : stationary flow simulations (RANS), mechanical simulations (FEM) and time-  
 139 linearized simulations (LRANS). Finally, aerodynamic behaviour and structural dynam-  
 140 ics of the fan are deduced and its aeroelastic stability is assessed.

## 141 2. ECL5 Description

### 142 2.1. Design approach

143 Based on an initial design [15], the final design was obtained with the use of a  
 144 modularly coupled design chain, including a parametric blade geometry generator,  
 145 automatic meshing, a steady RANS solver, and structural FEM simulations. The fan  
 146 geometry fulfils the following design objectives:

- 147 • Blade number of 16 (lowest blade count in technology demonstrators as shown  
 148 above).
- 149 • Fan diameter 508 mm to enable integration into test facility PHARE-2, blade root  
 150 compatible to existing disk from Project ENOVAL [16].
- 151 • (Fan-only) Aerodynamic design point at peak efficiency with a pressure ratio of  
 152 1.36, mass flow density maximum of 200 kg/s/m<sup>2</sup> and a rotation speed of 11000  
 153 rpm.
- 154 • Near sonic relative tip Mach number at design point.
- 155 • (Fan-only) Isentropic efficiency exceeding 94% at design point.
- 156 • At peak pressure of design speed no flow separation at the trailing edge.
- 157 • Peak efficiency at 105% speed not lower than 92% (transonic speedline).

<sup>4</sup> image sources: a) <https://www.additivemanufacturing.media/mission-critical/>, b) <https://www.air-cosmos.com/article/rolls-royce-tests-ultrafan-low-pressure-system-592> ; image flipped

- 158 • Nominal tip clearance  $\sim 1$  mm (1.1% tip chord) to ensure stall inception and surge  
159 experiments without casing contact, future experiments are planned with further  
160 reduced tip clearance.  
161 • The fan will be fabricated without integration of a metallic leading edge.

162 For the OGV, no specific design criteria were set except for a minimization of  
163 (numerical) corner separation at highly loaded conditions and minimum losses at design  
164 point. The blade number was fixed to 32 in the optimization process and reduced to 31  
165 for the final design to avoid the establishment of planar acoustic interactions.

166 Stage inlet and outlet geometry is similar to previous installations [16]. Same applies  
167 to the casing geometry in the fan section. The OGV is located far downstream of the  
168 fan to minimize interactions as the focus of the research project lies on the fan. As the  
169 facility comprises only a single flow channel, engine representative OGV aerodynamics  
170 are not intended, merely axial stage outflow and homogeneous radial conditions are  
171 required to ensure detailed performance analysis and to enable future research projects  
172 with fundamental background on noise generation.

173 The development process is described in detail in Pagès [17]. The hubline from  
174 nosecone to OGV outlet was open for optimization. A section of the design is presented in  
175 Figure 3. Figure 4 shows the blade profiles at different span heights, clearly emphasizing  
176 the transonic blade design at the fan tip and the wide chord geometry around midspan.  
177 At the hub, the relative tangential velocity and the rotational speed have the same  
178 direction at the trailing edge, which is necessary to meet the design criteria laid out  
179 above but creates a challenging flow field with high swirl velocities upstream the OGV.

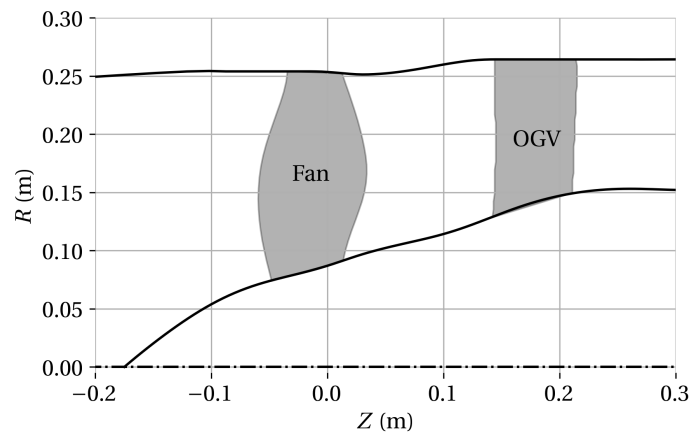


**Figure 3.** Section of ECL5 fan stage

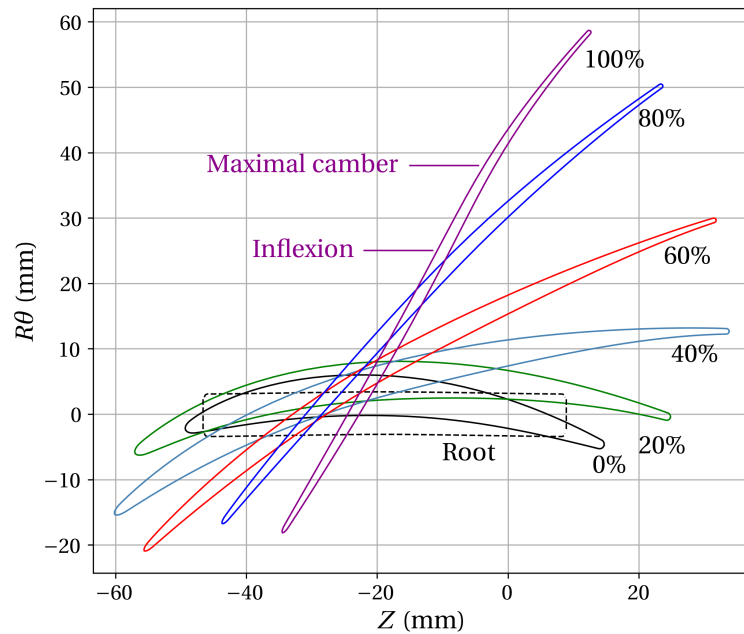


**Figure 4.** Fan profiles at different span heights

180 The tip clearance in dependence of the rotation speed is presented in Table 1:

**Table 1.** Tip clearance as predicted by FEM-Model (tip chord = 90 mm)

Rotation speed (100% = 11000 rpm)	Tip Clearance (mm)		Tip Clearance (% tip chord)	
	Leading edge	Trailing edge	Leading edge	Trailing edge
0%	1.00	1.50	1.11	1.67
50%	0.98	1.30	1.09	1.45
80%	0.87	1.12	0.97	1.25
100%	0.78	0.99	0.87	1.10
105%	0.77	0.92	0.86	1.02

## 181 2.2. Fan composite structure

182 The blade is exclusively made of unidirectional carbon fibres and epoxy composite  
 183 plies stacked into a laminate with intentional ply orientations . A ply is considered to be  
 184 made of orthotropic material. The three material orthotropy directions are defined locally  
 185 as follows : direction 1 is the orientation of the carbon fibres, direction 2 is orthogonal  
 186 to direction 1 within the ply and direction 3 is orthogonal to the ply. The constitutive  
 187 law of the composite material is described classically by nine constants listed in Table 2  
 188 (indicated by composite manufacturer).

**Table 2.** Material properties

$\rho$	$E_1$	$E_2 = E_3$	$G_{23}$	$G_{12} = G_{13}$	$\nu_{23}$	$\nu_{12} = \nu_{13}$
1560 kg/m <sup>3</sup>	123.0 GPa	9.3 GPa	5.0 GPa	4.5 GPa	0.3	0.26

189 The maximum thickness of the blade (at the root) is 13.3 mm. The thickness of a ply  
 190 is 0.15 mm so the maximum number of plies is 88. The internal structure is symmetric  
 191 with respect to the laminate midplane to minimize the coupling of in-plane and out-  
 192 of-plane movements. Each point of the midplane is associated with a number of plies  
 193 defined by the blade local thickness. Plies are ranked by their size from largest to smallest  
 194 (see Figure 5).

195 For the design process, plies have been divided in two families. The 18 largest plies  
 196 are called blade plies and the others - the smallest - are called core plies. To reduce the

197 number of degrees of freedom for the design, orientation of core plies is set considering  
 198 half a blade to the sequence  $((0^\circ/90^\circ)_6(0^\circ/90^\circ/0^\circ)_4(0^\circ/0^\circ))_s$ , with  $0^\circ$  defined as the  
 199 radial direction. Their influence on global elastic properties is minor and they mainly  
 200 contribute in thickness adjustment. Thus the total number of fibre orientations to define  
 201 is set to 18. These orientations are listed in Table 3. The orientation of a ply is defined as  
 202 illustrated in Figure 5b. The orientation is imposed on a chosen point at the root of the  
 203 blade. Local orientation along the blade is determined by the draping of the surface [18].

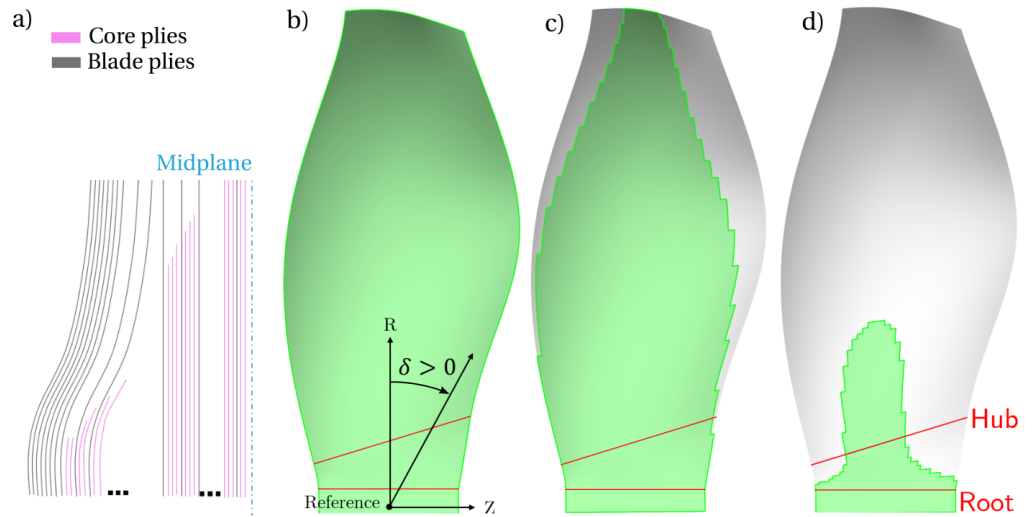


**Figure 5.** Plies of ECL5 Fan (colored in green) (a) Plies alternation (b) Ply 1 - blade: wrap (c) Ply 6 - blade (d) Ply 19 - core

204 The manufacturing process consists of three steps. First, each pre-impregnated ply  
 205 is cut to the pre-defined shape. Secondly, the plies are stacked into two half-molds. Then  
 206 both molds are pressed together before heating to start the polymerisation process of  
 207 epoxy.

208 The plies are stacked in a particular way to improve the manufacturing process and  
 209 final resistance to delamination. It is made of an alternation of blade plies and core plies  
 210 as illustrated in Figure 5a. One particular feature is that Ply 1 (the largest, Figure 5b)  
 211 is put at the external surface of the blade. Thus, the external surface is composed of only  
 212 one ply and has a very low surface roughness without any sharp step.

Ply	1	2	3	4	5	6	7	8	9
Orientation	$45^\circ$	$-45^\circ$	$-15^\circ$	$-30^\circ$	$15^\circ$	$-15^\circ$	$70^\circ$	$0^\circ$	$0^\circ$
Ply	10	11	12	13	14	15	16	17	18
Orientation	$-15^\circ$	$0^\circ$	$0^\circ$	$60^\circ$	$-60^\circ$	$0^\circ$	$0^\circ$	$60^\circ$	$-60^\circ$

**Table 3.** Blade plies orientation

### 213 3. Modelling strategies

#### 214 3.1. Aerodynamics

215 For aerodynamic simulations, a structured mesh has been created using AutoGrid<sup>5</sup>.  
 216 A single passage of the fan domain contains 3.5 Million cells, with 141 layers in radial  
 217 direction. 41 layers are used in the tip gap. The OGV domain contains 1.7 Million cells,  
 218 with 101 layers in radial direction and no tip gap. Fan meshing is illustrated in Figure 6.

219 Stationary flow simulations have been conducted with the RANS solver FineTurbo  
 220 <sup>6</sup>. The wall resolution of this mesh is below  $y^+ = 1$  for design conditions. A  $k - \omega$

<sup>5</sup> <https://www.numeca.com>

<sup>6</sup> <https://www.numeca.com>

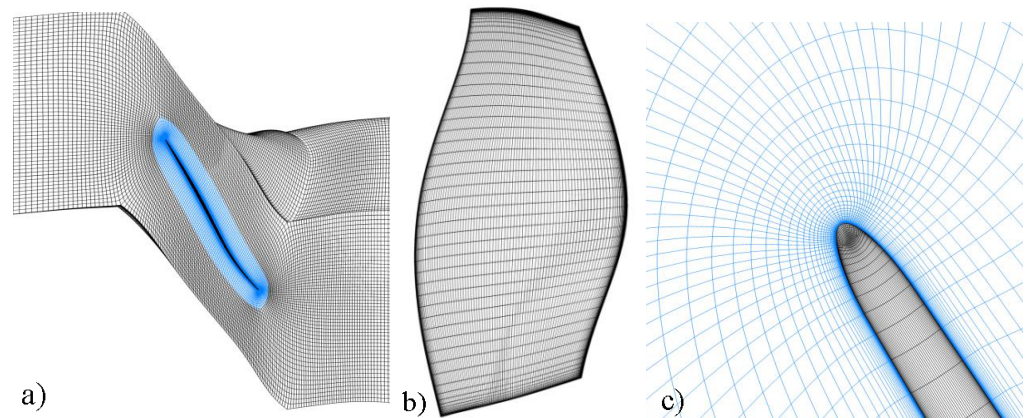


**Figure 6.** Views of structured mesh for aerodynamic simulations (a) Blade to blade (b) Meridional (c) O-mesh around the leading edge and the matching tip-clearance mesh

221 SST turbulence model is used for the simulations presented in the following. This  
 222 methodology was validated in a study on a comparable low-speed fan for the operating  
 223 range between choke and peak-pressure [16]. A study on mesh-convergence is presented  
 224 in [17].

### 225 3.2. Mechanics

226 FEM solve Ansys has been used for mechanical simulations<sup>7</sup>. The simulation do-  
 227 main and boundary conditions are presented in Figure 7a. A cyclic symmetry condition  
 228 is imposed on the faces of the disk sector (in purple) since fan is supposed to be tuned  
 229 and all blades identical. The shaft of the test facility is not modeled. To represent the  
 230 contact between the disk and the shaft, the disk is clamped in the blue area and the axial  
 231 displacement is set to zero in the green area. The aerodynamic pressure field is imposed  
 232 on the red surface. Static simulations include large deflection.

233 The blade composite laminate is modelled by a hexaedric 3D mesh (Ansys ACP<sup>8</sup>)  
 234 and dedicated procedure to model the ply alternation. To reduce the mesh size, a stack  
 235 of plies is modelled with a equivalent element. Each half-thickness is modelled by an  
 236 equivalent element (see Figure 7b) with orthotropic properties which are homogenized  
 237 from classical laminate theory [19].

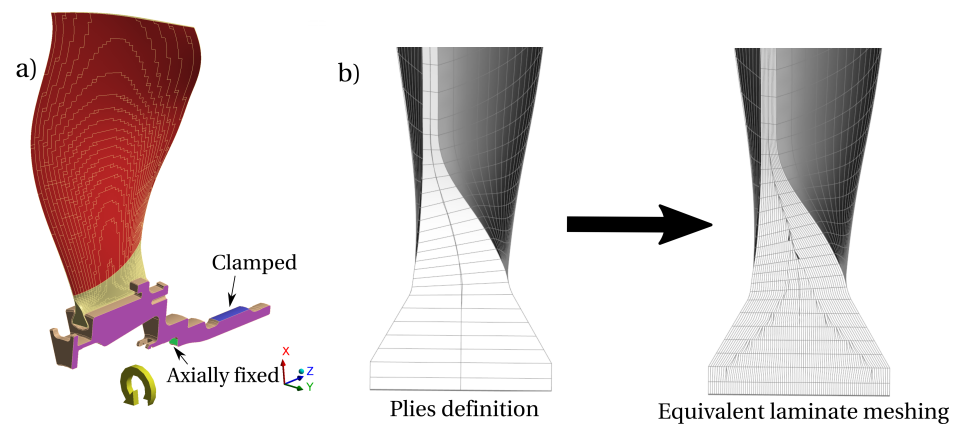


**Figure 7.** Mechanical model (a) Boundary conditions (b) Blade thickness meshing

<sup>7</sup> <https://www.ansys.com/products/structures/ansys-mechanical>

<sup>8</sup> <https://www.ansys.com/products/structures/composite-materials>

### 238 3.3. Aeroelasticity

#### 239 3.3.1. Energy method

240 Aeroelastic stability is investigated with the energy method [20]. This approach is  
 241 based on the assumption that flow fluctuations do not affect structural dynamics and  
 242 are linear with the vibration amplitude. It consists in two steps. First, eigenmodes and  
 243 natural frequencies are determined. Secondly, an unsteady flow simulation is performed  
 244 to compute the harmonic variations of the flow caused by the vibration. Aeroelastic  
 245 stability is determined by the energy transfer from the structure to the flow. It is assessed  
 246 by pressure force work  $W$  per vibration cycle. For a positive work ( $W > 0$ ), the blade  
 247 releases energy to the fluid so that vibrations are damped. For a negative work ( $W < 0$ ),  
 248 energy is transferred from the fluid into the structure, thus exciting the blade vibration  
 249 and leading to aeroelastic instability. In agreement with industrial convention, the  
 250 aerodynamic damping value is defined in the following as :

$$\zeta = \frac{W}{4\pi E_k} = \frac{W}{2\pi M_0 \omega_0^2} \quad (1)$$

251 with the modal kinetic energy  $E_k$  of the travelling wave, the modal mass  $M_0$  and the  
 252 vibration angular frequency  $\omega_0$ .

#### 253 3.3.2. Time-linearized simulations

254 The isolated fan is considered for the stability study according to common practice  
 255 for fan flutter studies based on self-excitation [1,21,22]. The OGV is one chord distant  
 256 downstream of the fan so its potential influence is significantly reduced.

257 To assess the stability of the fan, a time-linearized method (LRANS) is used. Based  
 258 on the assumption of small harmonic perturbations, the coordinates of the grid vertices  
 259 as well as the flow solution can be decomposed in a steady part and a time dependent  
 260 harmonic perturbation. These two parts are simulated separately.

261 The steady flow necessary for LRANS simulations is obtained with the compressible  
 262 RANS solver elsA<sup>9</sup>. The solver relies on cell-centered finite volume method on multi-  
 263 block structured grids. Convective fluxes are obtained with Jameson scheme with  
 264 artificial dissipation. The turbulence is modeled by  $k - \omega$  Kok model with vorticity-  
 265 based computation of turbulent kinetic energy production. A single passage of the fan  
 266 domain is reduced to 2.3 Million cells, with 101 layers in radial direction. 21 layers are  
 267 used in the tip gap. The wall resolution remains below  $y^+ = 1$ . A comparison of the  
 268 steady state results to those obtained with FineTurbo was carried out and showed few  
 269 disparities, resulting in differences lower than 0.3% in total pressure ratio and 0.3% in  
 270 isentropic efficiency for the studied operating points.

271 The unsteady flow is obtained with the solver Turb'Lin [23]. The solution is obtained  
 272 in the frequency domain. This vertex-centered LRANS solver has been validated for  
 273 transonic separated flows [23,24]. The turbulence model is linearized (see [25] for  
 274 comparison of results with frozen turbulence assumption). Upstream and downstream  
 275 of the fan, the mesh was extended by numerous fan diameters with strongly reduced  
 276 axial resolution to attenuate acoustic reflections.

## 277 4. Results

### 278 4.1. Aerodynamic characteristics

279 Stage characteristics of steady RANS calculations, throttled via static pressure at the  
 280 stage outlet are presented in Figure 8. It can be seen that overall peak efficiency is well  
 281 located at the 100% speedline at a point where the total pressure characteristic is almost  
 282 flat. For high speedlines above 100% of design speed, choke occurs in the fan, otherwise  
 283 it occurs in the OGV. Towards low mass-flow the speedlines are rolled over and limited  
 284 by numerical convergence. This is comparable to the case presented by Rodrigues *et al.*

<sup>9</sup> <http://elsa.onera.fr/>

285 [16], which has shown that through application of a choked nozzle far downstream the  
 286 numerical stability limit can be further extended but still not reaching the stability limit  
 287 of the experiment. At highly throttled conditions the performance in experiments are  
 288 expected to significantly deviate from numerical results. In this paper, five operating  
 289 points representative of the different flow topologies and limits are presented. OP-A is  
 290 the design point, OP-B is the maximum pressure ratio and OP-C presents a choked flow  
 291 at 100% speed. OP-D and OP-E are operating points near the maximum pressure ratio at  
 292 80% speed.

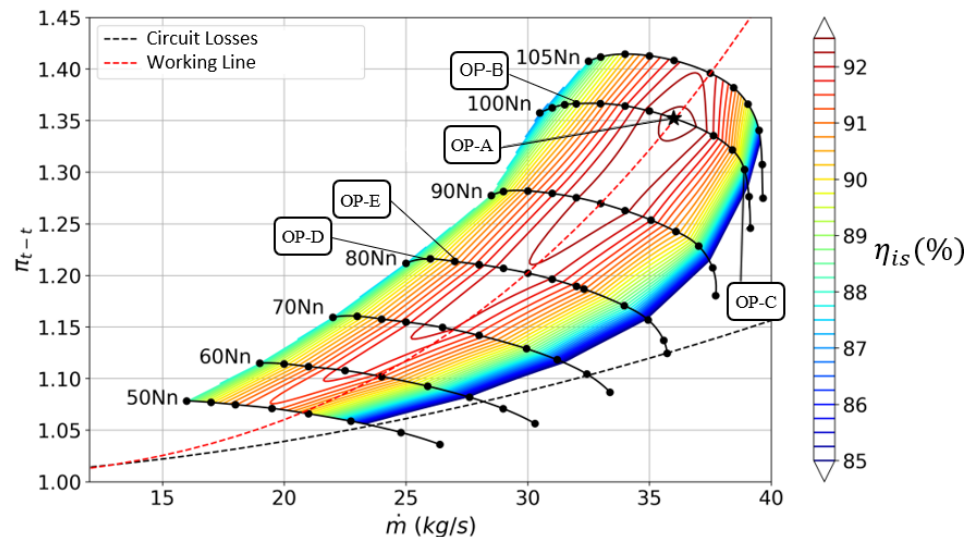


Figure 8. Stage compressor map with operating points of interest

293 A detail of the 100% speedline is given in Figure 9, showing pressure and efficiency  
 294 characteristics as well as radial profiles at rotor exit<sup>10</sup>. In a wide range between OP-B  
 295 and OP-C (representing 19% of design mass flow, depicted cyan in Figure 9), the fan  
 296 produces a flat efficiency characteristic above 88%. The evolution between the lowly  
 297 throttled operating point OP-C and the higher throttled conditions shows that the fan  
 298 is barely affected between hub and midspan. The maximum pressure ratio is observed  
 299 near midspan and throttling increases loading of the blade tip. At design point OP-A, the  
 300 efficiency profile is almost constant between 20% and 80% span. Influence of tip-leakage  
 301 flow is observed between 85% and 100% span for all shown conditions.

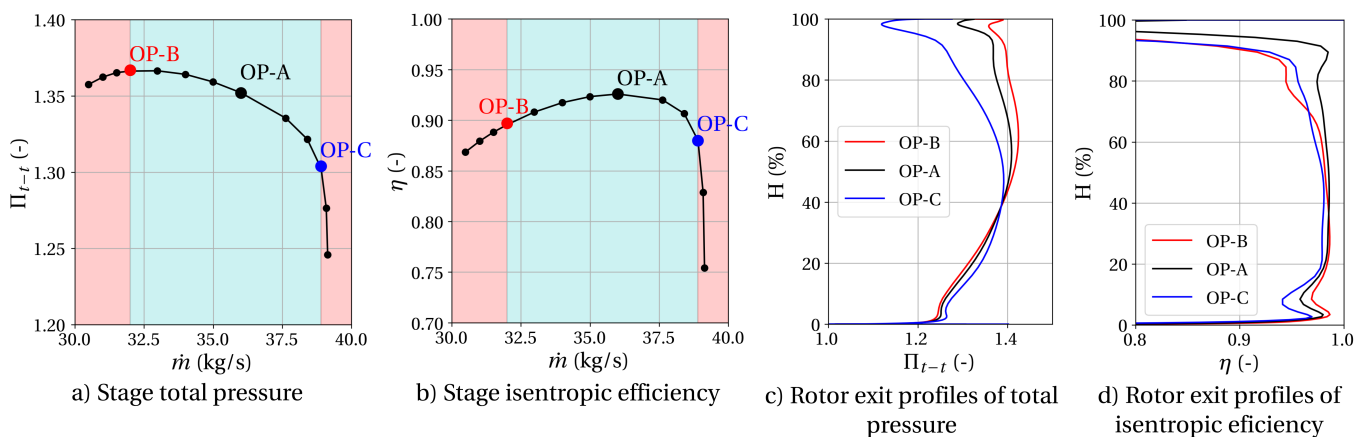


Figure 9. Detail of flow conditions at different operating points at 100% speed

<sup>10</sup> Aerodynamic simulations for 1.5mm constant tip clearance, fabricated fan has tip clearance according to Table 1

302 In Figure 10 the flow structure is presented in more detail for design point OP-A.  
303 Isentropic Mach number distribution on the suction side shows the shock structure  
304 from midspan and emphasizes the reduced loading at blade tip. Surface streamlines are  
305 homogeneous without indications for flow separations but moderate radial migration  
306 towards the trailing edge. The blade-to-blade view of the relative Mach number and  
307 radial velocity at 95% span indicates low blockage in the tip region and a clearly depicted  
308 tip leakage vortex that mildly interacts with the shock.

309 This situation changes at maximum pressure condition OP-B, where the pre-shock  
310 Mach number strongly increases, and the surface streamlines show signs of boundary  
311 layer separation between 70% span and the casing. Also, radial migration is accen-  
312 tuated leading to low relative Mach numbers below 0.2 at the trailing edge at lower  
313 channel heights. The blade-to-blade view depicts a strong blockage zone enclosed by the  
314 emphasized tip-clearance flow. Here, a stronger interaction with the shock is indicated.

315 The same illustration is given for the maximum pressure point at the 80% speedline  
316 OP-D. Here, the flow is mostly subsonic. The supersonic zone (without shock) in  
317 isentropic Mach number distribution is due to the circumvention of the leading edge.  
318 Surface streamlines indicate significant local backflow at the leading edge for higher  
319 channel heights. The blockage region at the fan tip is more severe than at design speed  
320 with a widely inclined zone of negative radial velocity. Radial flow migration is highly  
321 accentuated at this condition, particularly close to the casing. However, due to low  
322 relative velocity, the amplitude of radial velocity close to the casing is lower than for the  
323 higher speedline.

## 324 4.2. *Mechanics*

### 325 4.2.1. Static mechanics

326 Hot shapes of the fan blade were determined for each speedline along the work-  
327 ing line. Due to the use of anisotropic properties of composite, the maximal blade  
328 displacement is 1.15 mm at maximal speed corresponding to 1.0% of the chord. It is  
329 comparable to the optimization presented by Schmid *et al.* [13]. Maximum static stress in  
330 fiber direction does not exceed 17% of elastic limit. Static stress is then low compared to  
331 elastic limit which allows sufficiently high level of dynamic stress during experimental  
332 campaign.

### 333 4.2.2. Mode Shapes

334 Concerning synchronous excitation phenomena, intake distortions are the predomi-  
335 nant sources. The potential effects of the OGV are negligible because of the axial distance  
336 from the fan, of more than one chord. Experience on similar configurations shows that  
337 above the 6<sup>th</sup> engine order, forced response amplitudes are negligible [16,26]. At 105%  
338 of nominal rotation speed, the 6<sup>th</sup> engine order frequency is 1155 Hz. Mode 3 and Mode  
339 4 frequencies are respectively around 900 Hz and 1500 Hz at maximal rotation speed so  
340 only the first three modes are considered in the following.

341 Modal data are presented only for positive nodal diameters because they are identi-  
342 cal for both co-rotative and contra-rotative modes. Modal frequencies are given in Figure  
343 11a for each nodal diameter (ND). Frequency variations are less than 2% except for low  
344 nodal diameters between modes of the same family. Mode 1ND0 frequency is lowered  
345 by 9% compared to the other NDs. Mode 2ND1 and Mode 3ND1 frequencies are also  
346 reduced by respectively 12% and 14%. To assess for mode shape variations between  
347 nodal diameters, the Mode Assurance Criterion (MAC) is used [27]. For each mode, the  
348 mode shape is compared to its ND8 counterpart. MAC is equal to 1 if the mode shapes  
349 are identical, 0 if they are inconsistent. MAC is represented in Figure 11b. Except for  
350 ND1, the three modes are superimposed at 1. Modes 2ND1 and 3ND1 are very different  
351 from other NDs due to high disc contribution. Mode 1ND0 mode shape is comparable  
352 even if its frequency is slightly different. These significant variations between nodal  
353 diameters have to be taken into account for aeroelastic studies. Furthermore the accuracy

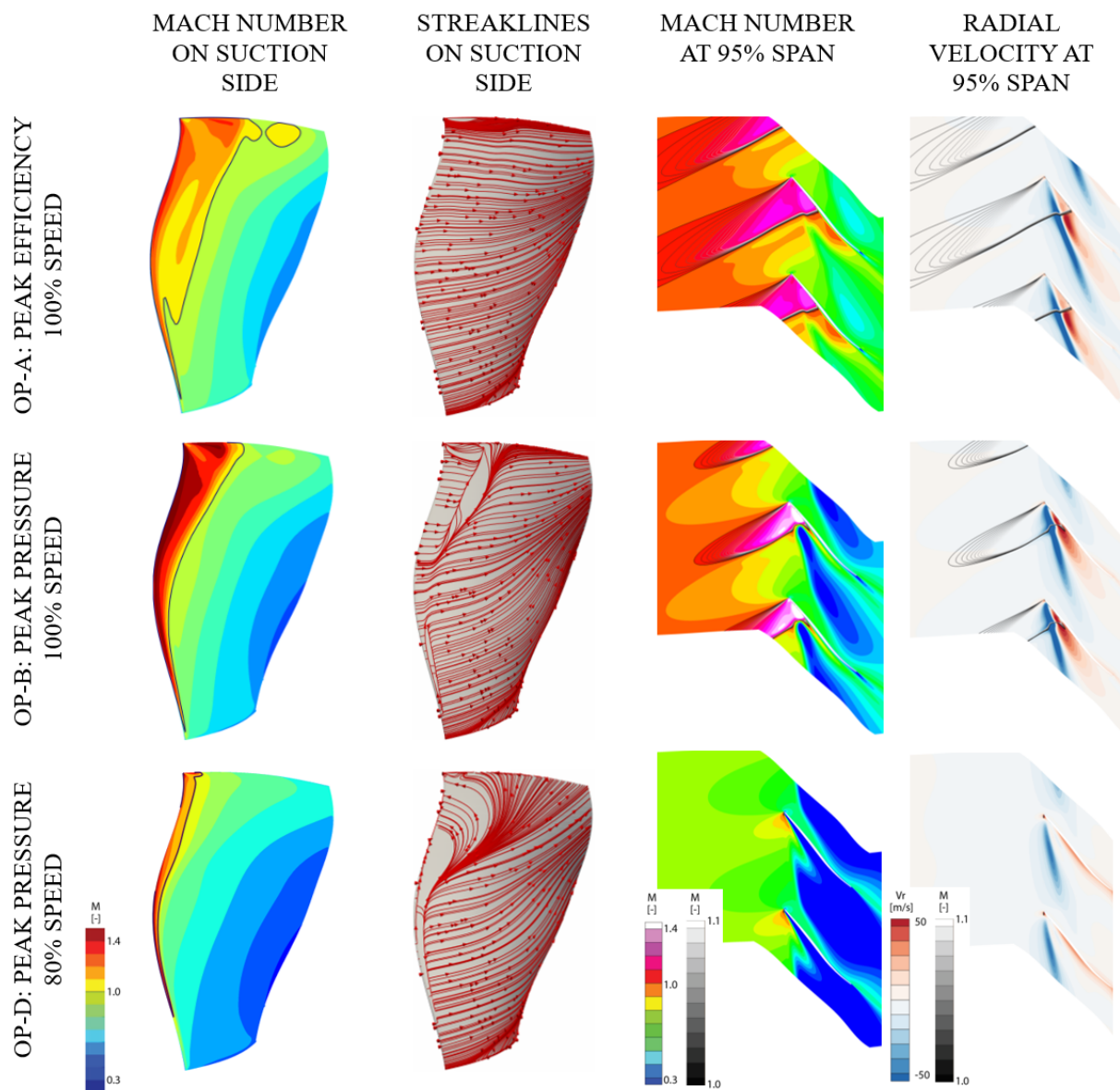


**Figure 10.** Detail of flow conditions at different operating points

354 of the prediction can be affected by support stiffness and gyroscopic effects. Thus the  
 355 choice to model the disk without the shaft could have an important impact on this nodal  
 356 diameter (ND1) and must be addressed in further studies.

357 Mode shapes at ND2 are shown in Figure 12. ND2 is representative of all nodal  
 358 diameters except ND1. Mode 1 is a bending mode with very low torsional component.  
 359 The displacement is almost only circumferential without axial component. Mode 2  
 360 shows a pronounced torsional component at the blade tip which is known to be critical  
 361 for fluid-structure interactions [6,28]. Mode 3 represents a torsional mode with torsional  
 362 center positioned at half-chord at midspan and at the leading edge at the tip.

363 Mode shapes at ND1 are shown in Figure 13. As identified in Figure 11b, Mode  
 364 2ND1 and Mode 3ND1 are very different from their other equivalent NDs. In particular,  
 365 the mode shape of 3ND1 is closer to Mode 2 than Mode 3.

#### 366 4.2.3. Campbell diagram

367 The Campbell diagram obtained for the fan is presented in Figure 14. The crossings  
 368 of the different modes with EO lines are highlighted. Modal frequencies were adjusted

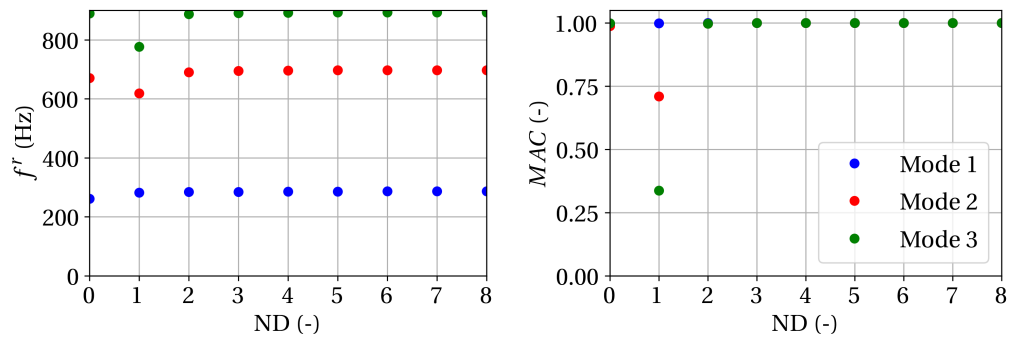


**Figure 11.** Nodal diameter influence on modes at 100% speed (a) Frequency (b) MAC in comparison with ND8

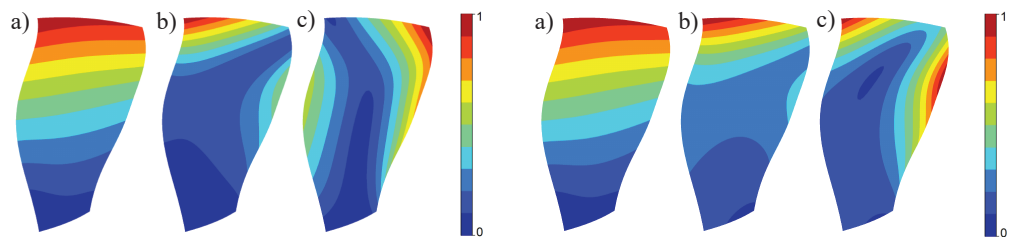


**Figure 12.** Normalized modal displacement amplitude at ND2 (a) Mode 1 (b) Mode 2 (c) Mode 3

**Figure 13.** Normalized modal displacement amplitude at ND1 (a) Mode 1 (b) Mode 2 (c) Mode 3

369 during the design process - thanks to carbon fiber orientations - to prevent crossings  
 370 above 100% speed. These are sufficiently distributed in frequency to enable safe tests - i.e.  
 371 without resonance caused fatigue - at low part-speed ( $\sim 50\%$ ), high part-speed ( $\sim 80\%$ )  
 372 and full speed (100% and above). Experience shows that the predicted frequencies  
 373 are slightly higher than those of manufactured blades. Fans produced by the same  
 374 manufacturer show that the frequency predictions are nearly 5% higher for torsional  
 375 modes [16,26]. Moreover, in previous experimental campaigns, crossing with engine  
 376 orders higher than 3 never prevented speedline exploration. Hence, the 80% speedline  
 377 should be safely investigated despite the crossing of Mode 3.

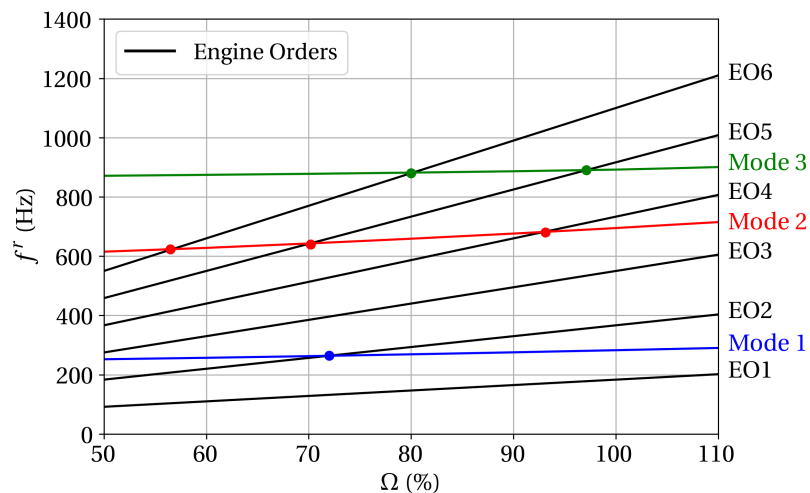


**Figure 14.** Campbell diagram at ND2

### 378 4.3. Overall stability analysis

#### 379 4.3.1. Strategy

380 To be representative of industrial configurations and to enable comprehensive  
 381 experimental campaigns, it is necessary that the fan presents stable operating conditions  
 382 at every planned experimental rotation speed. An exhaustive review would be to test  
 383 every nodal diameter of every mode at each rotation speed. Even with LRANS method,  
 384 this exceeds the scope of a design study. The systematic stability analysis is restrained to  
 385 4 operating points. The design point OP-A serves as reference and must be stable in any  
 386 case. OP-B, OP-C, and OP-D are representative of the different flow limits (see Figure 8).

387 Flutter events detected on modern fans mostly involve first bending mode at low  
 388 nodal diameter [1,21,22]. However it has been shown by Stapelfeldt and Brandstetter [6]  
 389 that torsional mode shapes could lead to aeroelastic instability for a convective mecha-  
 390 nism denoted as Non-Synchronous Vibration. Thus all three modes were investigated.  
 391 Table 4 gives tip reduced frequencies (see Equation 2) based on chord and upstream  
 392 relative velocity at both considered speeds.

$$k_r = \frac{f^r c}{U^{tip}} \quad (2)$$

393 To reduce the number of aeroelastic configurations to simulate, only even numbers  
 394 of nodal diameters were simulated in a first step. The nodal diameters  $\pm 1$  were added  
 395 because their aeroelastic behaviour cannot be deduced from other nodal diameters due  
 396 to their mode shape (see Figures 12 and 13). Odd nodal diameters were simulated if  
 397 discontinuities in aerodynamic damping curves were observed.

#### 398 4.3.2. Aerodynamic damping

399 Figures 15 and 16 show the aerodynamic damping ratio  $\zeta$  as function of the nodal  
 400 diameter at operating points OP-A to OP-D. The minimal values of each curve are  
 401 gathered in Table 5. At OP-A, the design point, aerodamping is always positive and the  
 402 minimal value reached is 1.38%. Mode 1 aerodamping variations as function of nodal  
 403 diameter are smooth for every operating point. Smallest value occurs between ND0  
 404 and ND2 and it exceeds 5% for high NDs. For every operating point studied, Mode 1  
 405 is globally more stable than Mode 2 or Mode 3, especially at high NDs. Aerodamping  
 406 curves for Mode 2 and Mode 3 are more erratic and minimal values are reached for  
 407 various NDs. Only one point was found to be unstable : Mode 2ND5 at OP-D. Among  
 408 all other simulated configurations, the aerodamping is always higher than 0.69%.

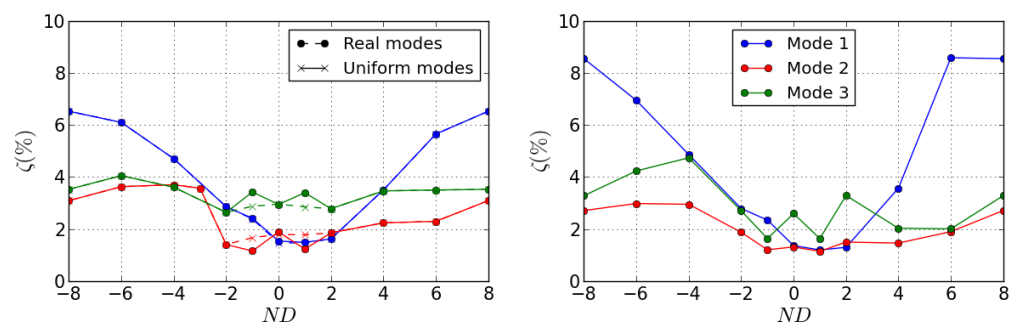
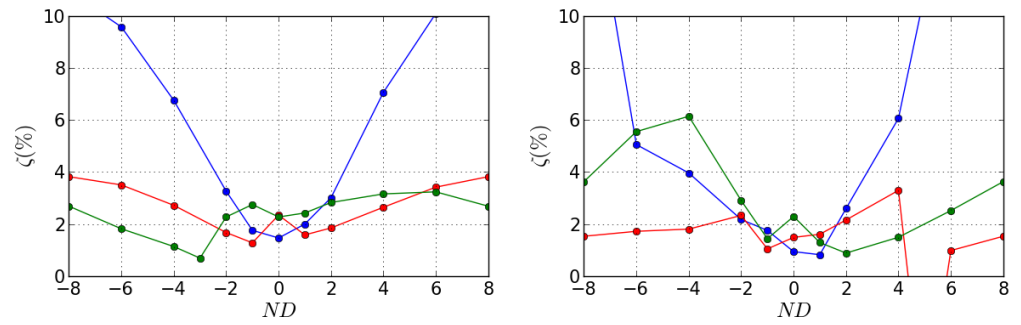


Figure 15. Aerodynamic damping as function of nodal diameter (a) OP-A (b) OP-B

Table 4. Reduced frequency on working line (ND8)

Speedline	80%	100%
Mode 1	0.09	0.08
Mode 2	0.22	0.19
Mode 3	0.30	0.24



**Figure 16.** Aerodynamic damping as function of nodal diameter (a) OP-C (b) OP-D

**Table 5.** Minimum of aerodynamic damping

Operating point	Mode 1	Mode 2	Mode 3
OP-A (100%, 36.0 kg/s)	1.50%	1.38%	2.64%
OP-B (100%, 32.0 kg/s)	1.20%	1.15%	1.64%
OP-C (100%, 38.9 kg/s)	1.47%	1.28%	0.69%
OP-D (80%, 26.0 kg/s)	0.83%	-5.60%	0.89%

#### 4.3.3. Influence of mode frequency and mode shapes on damping

Abrupt changes are observed in damping curves. Among possible reasons, one could be the change of mode shape and frequency for low nodal diameters (see Figure 11). This dependency was quantified at OP-A in Figure 15a. Aerodynamic damping is computed with the same frequency and mode shape from ND8 (Uniform modes) which is similar to ND2 shown Figure 12. It is compared to aerodynamic damping obtained with modes from FEM (Real modes). Resulting curves with uniform modes are smoother. Aerodamping is mostly impacted at mode  $2ND \pm 1$  and mode  $3ND \pm 1$  whose modal shapes and frequencies were very different of other NDs. Mode  $1ND_0$  has a shift in frequency of 9%, however the impact on the stability behavior is marginal. Then erratic changes observed between nodal diameters  $-2$  and  $2$  are mostly due to mode shapes variations.

#### 4.4. Instability analysis

Upstream and downstream acoustic conditions can produce discontinuities in stability behaviour of the blades [29]. On the operating points studied, numerous switches of cut-on/cut-off conditions can be observed but only three discontinuities related to acoustic behaviour that could lead to instability were identified :

- For Mode  $2ND-3$  at OP-A, the stability curve is flat at each side of the discontinuity and the fan remains stable (see Figure 15a).
- For Mode  $3ND-3$  at OP-C, the stability reaches a minimum but the fan remains stable (see Figure 16a).
- For Mode  $2ND5$  at OP-D, the fan is predicted unstable (see Figure 16b). The stability behaviour for ND4 to ND6 is investigated in the following .

##### 4.4.1. Aeroelastic instability of Mode 2 at OP-D

For Mode  $2ND5$  at OP-D, the fan is predicted unstable and the aerodamping reaches a negative minimum at  $\zeta = -5.6\%$ . The local work at the surface of the blade, normalized like the global work by  $U = 4\pi E_k$  (see Equation 1), is plotted Figure 17 for ND4 to ND6. The local work is mostly located at the tip of the blade because of the mode shape (see Figure 12b). Corresponding flow fluctuations at ND5 are more than one order of magnitude higher than for adjacent nodal diameters. For example, if the displacement is arbitrarily set to 1.0% of the chord at the tip, the maximal pressure fluctuations will be 65% of inlet static pressure. At ND5, fluctuations cannot be analyzed quantitatively

441 because it is out of the hypothesis of small perturbations on which the linearized method  
442 is based.

443 At ND4 and ND6, the hypothesis of small perturbations remains valid and the  
444 work distribution can be analysed. Figure 17 shows that both suction side and pressure  
445 side are equivalently involved in overall stability of the blade. The local work patterns  
446 between ND4 and ND6 on the pressure side are similar but of opposite sign. On the  
447 suction side, patterns are different. At ND4, the work is negative then positive near  
448 the leading edge with high values. Whereas the work is mildly positive at ND6 on a  
449 large area. This important change of behaviour between these nodal diameters indicates  
450 resonance, which is reached near ND5. Damping value obtained at ND5 is questionable  
451 due to resonance. However it still shows that instability could be expected at these  
452 operating conditions which must be investigated with caution during experiments.

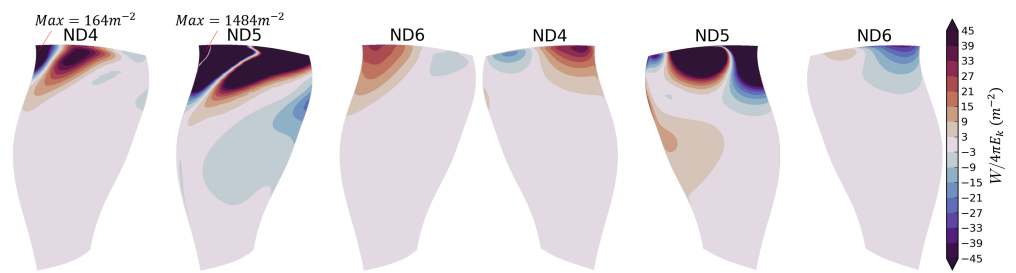


Figure 17. Local work at OP-D for Modes 2ND4 to 2ND6 (left) Suction side (right) Pressure side

#### 453 4.4.2. Acoustic propagation conditions

The propagation conditions [30] of Mode 2 at OP-D are presented in Figure 18. This figure gives an understanding of acoustics in the duct. An acoustic pressure wave generated by a vibrating fan can propagate axially if the frequency in the steady frame of reference  $f^s$  is higher than a frequency  $f^{cut}$  called cut-off frequency.  $f^s$  is determined by the Equation 3.

$$f^s = |f^r + \Omega ND| \quad (3)$$

with  $f^r$  the frequency in the rotating frame of reference (i.e. the modal frequency). On the assumption of uniform flow in radial direction, rigid body flow and hard-walled duct, the acoustic cut-off frequency for a subsonic axial flow can be estimated according to Hellmich and Seume [30] as :

$$f^{cut} = \frac{k_r a}{2\pi} \left( \sqrt{1 - M_x^2} \pm M_\theta \right) \quad (4)$$

454 with  $M_x$  and  $M_\theta$  the axial and circumferential Mach number,  $a$  the sound speed and  
455  $k_r$  the radial modal wave number calculated from Bessel functions.  $M_x$  and  $M_\theta$  are  
456 determined by the mean value far upstream and downstream of the blade. Propagation  
457 conditions are shown in Figure 18 and were verified in linearized simulations results.  
458 Upstream, acoustic waves propagate for ND0 to ND6. Downstream, acoustic waves  
459 propagate at ND4 but neither ND5 nor ND6. At the opposite neither ND5 nor ND6  
460 propagates. Vibration patterns which fulfill this condition of being cut-on only in one  
461 axial direction are known to be critical for aeroelastic stability [4,31]. Discontinuity  
462 observed in the aerodamping curve (Figure 19) for OP-D seems to coincide with change  
463 of the acoustic propagation conditions shown in Figure 18.

#### 464 4.4.3. Influence of operating point

465 Aeroelastic stability is compared between OP-D and OP-E for Modes 2ND4 to 2ND6.  
466 At OP-E, the massflow is 3.8% higher than at OP-D and the leading edge separation  
467 size is reduced to 25% of the chord. The acoustic cut-off frequencies at OP-E are not

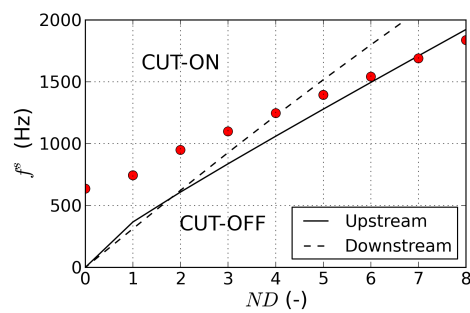


**Figure 18.** Mode 2 (red dots) acoustic conditions at OP-D et OP-E

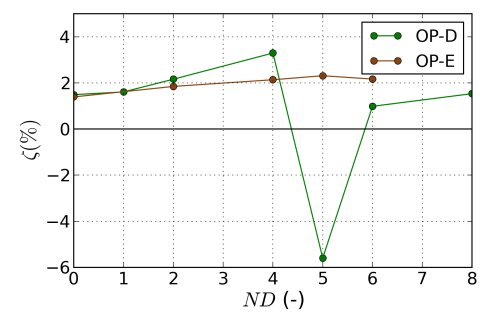


**Figure 19.** Mode 2 aerodynamic damping at OP-D and OP-E

468 shown in Figure 18 because the differences with OP-D (of less than symbol size) are  
 469 not significant compared to the model accuracy. It is verified in simulations that the  
 470 acoustic propagation conditions upstream and downstream for ND4 to ND6 are the  
 471 same for both operating points. The normalized local work distributions are presented  
 472 in Figure 20. Contrary to OP-D (see Figure 17), results show very little influence of the  
 473 nodal diameter at this operating point and only stabilizing aerodynamic damping higher  
 474 than 2.0% (see Figure 19). On the suction side, the work repartition looks like ND4 at  
 475 OP-D but with lower amplitude. Unlike results at OP-D, the work on the pressure side  
 476 is one order lower than on suction side. Here, the stability of the blade is driven by the  
 477 suction side. The shift of 3.8% in massflow leads to a stable system and suppresses the  
 478 strong influence of nodal diameter on fan stability. Thus, even if the acoustic conditions  
 479 are similar, the fan remains stable closer to the operating line. Based on the presented  
 480 study it is not clear if the acoustic conditions are the dominant driver for instability  
 481 or if a convective mechanism as described by Stapelfeldt and Brandstetter [6] leads to  
 482 aeroelastic lock-in (Non-Synchronous Vibrations). The latter case is not unlikely as the  
 483 ND5 pattern can be in resonance with a backward travelling aerodynamic disturbance  
 484 of wave-number 11 (aliased on a 16 blades rotor). This disturbance would propagate  
 485 with a speed of  $\approx 60\%$  of the fan speed in the absolute frame of reference which is well  
 486 in the range of reported convective disturbances [16] but it has not been investigated  
 487 before using time-linearized methods. Nevertheless, the detected instability at OP-D  
 488 does not prevent experimental exploitation of the speedline as it occurs only close to the  
 489 stall limit and in case of convective lock-in limit cycle oscillations are expected.

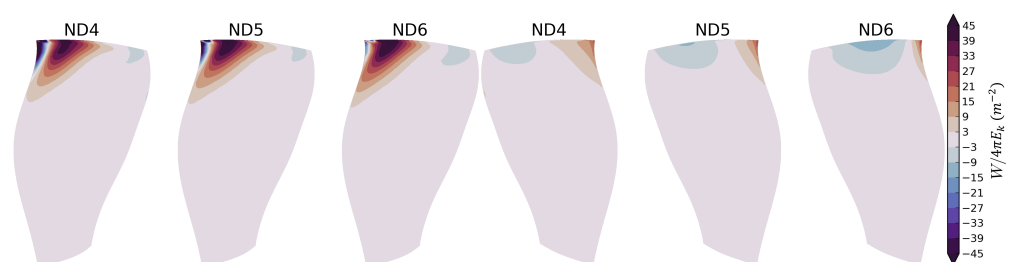


**Figure 20.** Local work at OP-E for Modes 2ND4 to 2ND6 (left) Suction side (right) Pressure side

## 490 5. Conclusions

491 A fan representative of modern UHBR fans was designed and presented as an  
 492 open test case. The fan blades are made of unidirectional carbon fibres and epoxy  
 493 composite plies. To enable an analysis of the dynamic behaviour, structural properties,  
 494 manufacturing process and ply orientations were presented.

495 The second mode of the fan has a significant torsional component at the blade tip  
 496 which makes it likely to be critical for fluid-structure interactions. Modes of a same

497 family vary significantly at low nodal diameters. The impact of this disparity was  
 498 quantified in aeroelastic studies. Fan stability was systematically investigated over  
 499 representative operating points with a time-linearized method. At nominal speed, no  
 500 aeroelastic instabilities were predicted. Thus, it will be possible to investigate highly  
 501 loaded operating conditions. At part-speed, a potential instability was identified at  
 502 throttled conditions and will be investigated in more details in future work. It was  
 503 shown that the instability area remains localized far from the operating line and it will  
 504 be in the focus of the planned experimental campaign which will start mid 2022.

505 **Author Contributions:** Valdo Pagès: conceptualization, methodology, investigation, writing-  
 506 original draft preparation, review and editing, visualization  
 507 Pierre Duquesne: conceptualization, methodology, investigation, writing-review, supervision  
 508 Stéphane Aubert: conceptualization, methodology, investigation, writing-review, supervision,  
 509 funding acquisition : CIRT  
 510 Laurent Blanc: conceptualization, methodology, investigation, writing-review, supervision  
 511 Pascal Ferrand: conceptualization, methodology, investigation, writing-review, supervision  
 512 Xavier Ottavy: conceptualization, methodology, investigation, writing-review, supervision, project  
 513 administration/funding acquisition: CleanSky N°864719  
 514 Christoph Brandstetter: conceptualization, methodology, investigation, writing-original draft  
 515 preparation, review and editing, visualization, supervision, project administration/funding acqui-  
 516 sition : CleanSky N°864719

517  
 518 **Funding:** This project has received funding from the Clean Sky 2 Joint Undertaking (JU) under  
 519 grant agreement N°864719. The JU receives support from the European Union’s Horizon 2020  
 520 research and innovation programme and the Clean Sky 2 JU members other than the Union. This  
 521 publication reflects only the author’s view and the JU is not responsible for any use that may be  
 522 made of the information it contains. . The development of the Open-Test-Case fan is supported by  
 523 CIRT (Consortium Industrie-Recherche en Turbomachine).

524 **Data Availability Statement:** The geometry, experimental results and available simulations  
 525 are accessible to European research institutes and international researchers upon negotiation.  
 526 Registration under [catana.ec-lyon.fr](http://catana.ec-lyon.fr).

527 **Acknowledgments:** The authors thank the continuous support of Safran Aircraft Engines, and  
 528 particularly the contribution of Laurent Jablonski during the design phase of the Open-Test-Case.

529 **Conflicts of Interest:** The authors declare no conflict of interest.

### 530 Abbreviations

531 The following abbreviations are used in this manuscript:

532	EO	Engine Order
	FEM	Finite Element Method
	LRANS	Linearized Reynolds-Averaged Navier–Stokes
	ND	Nodal Diameter
533	NSV	Non Synchronous Vibration
	OGV	Outlet Guide Vanes (Stator)
	OP	Operating Point
	RANS	Reynolds-Averaged Navier–Stokes
	UHBR	Ultra High Bypass Ratio

## References

1. Vahdati, M.; Cumpsty, N. Aeroelastic Instability in Transonic Fans. *Journal of Engineering for Gas Turbines and Power* **2015**, *138*, 022604. doi:10.1115/1.4031225.
2. Lee, B.H.K. Self-sustained shock oscillations on airfoils at transonic speeds. *Progress in Aerospace Sciences* **2001**, *37*, 147–196. doi:10.1016/S0376-0421(01)00003-3.
3. Dodds, J.; Vahdati, M. Rotating Stall Observations in a High Speed Compressor—Part I: Experimental Study. *Journal of Turbomachinery* **2015**, *137*, 051002. doi:10.1115/1.4028557.

4. Fiquet, A.L.; Vercoutter, A.; Buffaz, N.; Aubert, S.; Brandstetter, C. Acoustic resonance in an axial multistage compressor leading to non-synchronous blade vibration. Proceedings of Proceedings of ASME Turbo Expo 2020 & Turbomachinery Technical Conference and Exposition; ASME: London, UK, 2020.
5. Kielb, R.E.; Barter, J.W.; Thomas, J.P.; Hall, K.C. Blade Excitation by Aerodynamic Instabilities: A Compressor Blade Study. Proceedings of the ASME Turbo Expo 2003, collocated with the 2003 International Joint Power Generation Conference. American Society of Mechanical Engineers Digital Collection, 2003, Vol. Volume 4, pp. 399–406. doi:10.1115/GT2003-38634.
6. Stapelfeldt, S.; Brandstetter, C. Non-synchronous vibration in axial compressors: Lock-in mechanism and semi-analytical model. *Journal of Sound and Vibration* **2020**, *488*, 115649. doi:10.1016/j.jsv.2020.115649.
7. Lee, K.B.; Wilson, M.; Vahdati, M. Validation of a Numerical Model for Predicting Stalled Flows in a Low-Speed Fan—Part I: Modification of Spalart–Allmaras Turbulence Model. *Journal of Turbomachinery* **2018**, *140*, 051008. doi:10.1115/1.4039051.
8. Peters, A.; Spakovszky, Z.S.; Lord, W.K.; Rose, B. Ultrashort Nacelles for Low Fan Pressure Ratio Propulsors. *Journal of Turbomachinery* **2015**, *137*, 021001. doi:10.1115/1.4028235.
9. Wilson, M.J.; Imregun, M.; Sayma, A.I. The Effect of Stagger Variability in Gas Turbine Fan Assemblies. *Journal of Turbomachinery* **2006**, *129*, 404–411. doi:10.1115/1.2437776.
10. Lu, Y.; Green, J.; Stapelfeldt, S.C.; Vahdati, M. Effect of Geometric Variability on Running Shape and Performance of a Transonic Fan. *Journal of Turbomachinery* **2019**, *141*. doi:10.1115/1.4044676.
11. Zhai, Y.; Bladh, R.; Dyverfeldt, G. Aeroelastic Stability Assessment of an Industrial Compressor Blade Including Mistuning Effects. *Journal of Turbomachinery* **2012**, *134*. doi:10.1115/1.4007210.
12. Goerke, D.; Le Denmat, A.L.; Schmidt, T.; Kocian, F.; Nicke, E. Aerodynamic and Mechanical Optimization of CF/PEEK Blades of a Counter Rotating Fan. ASME Turbo Expo 2012: Turbine Technical Conference and Exposition. Volume 7: Structures and Dynamics, Parts A and B; ASME: Copenhagen, Denmark, 2012; pp. 21–33. doi:10.1115/GT2012-68797.
13. Schmid, T.; Lengyel-Kampmann, T.; Schimdt, T.; Nicke, E. Optimization of a carbon fiber composite blade of a counter-rotating fan for aircraft engines. Proceedings of 13th European Conference on Turbomachinery Fluid dynamics & Thermodynamics; European Turbomachinery Society: Lausanne, Switzerland, 2019.
14. Reiber, C.; Blocher, M. Potential of aeroelastic tailoring to improve flutter stability of turbomachinery compressor blades. Proceedings of 12th European Conference on Turbomachinery Fluid dynamics & Thermodynamics; European Turbomachinery Society: Stockholm, Sweden, 2017. doi:10.29008/ETC2017-180.
15. Rendu, Q. Modélisation des écoulements transsoniques décollés pour l'étude des interactions fluide-structure. phdthesis, Université de Lyon, 2016.
16. Rodrigues, M.; Soulat, L.; Paoletti, B.; Ottavy, X.; Brandstetter, C. Aerodynamic Investigation of a Composite Low-Speed Fan for UHBR Application. *Journal of Turbomachinery* **2021**, *143*, 101004. doi:10.1115/1.4050671.
17. Pagès, V. Conception du fan UHBR ECL5 pour une analyse des mécanismes d'interactions multi-physiques à l'origine du flottement. PhD thesis, Ecole Centrale de Lyon, 2021.
18. Wang, J.; Paton, R.; Page, J.R. The draping of woven fabric preforms and prepregs for production of polymer composite components. *Composites Part A: Applied Science and Manufacturing* **1999**, *30*, 757–765. doi:10.1016/S1359-835X(98)00187-0.
19. Barbero, E.J. *Finite Element Analysis of Composite Materials Using ANSYS®, Second Edition*; CRC Press, 2013.
20. Carta, F.O. Coupled Blade-Disk-Shroud Flutter Instabilities in Turbojet Engine Rotors. *Journal of Engineering for Power* **1967**, *89*, 419–426. doi:10.1115/1.3616708.
21. Sanders, A.J.; Hassan, K.K.; Rabe, D.C. Experimental and Numerical Study of Stall Flutter in a Transonic Low-Aspect Ratio Fan Blisk. *Journal of Turbomachinery* **2004**, *126*, 166–174. Publisher: American Society of Mechanical Engineers Digital Collection, doi:10.1115/1.1645532.
22. Aotsuka, M.; Murooka, T. Numerical Analysis of Fan Transonic Stall Flutter. Proceedings of the ASME Turbo Expo 2014: Turbine Technical Conference and Exposition. Volume 7B: Structures and Dynamics.; ASME: Düsseldorf, Germany, 2014; Vol. V07BT35A020. doi:10.1115/GT2014-26703.
23. Rendu, Q.; Philit, M.; Rozenberg, Y.; Labit, S.; Chassaing, J.C. Time-linearized and harmonic balance navier-stokes computations of a transonic flow over an oscillating bump. Proceedings of the 14th International Symposium on Unsteady Aerodynamics, Aeroacoustics & Aeroelasticity of Turbomachines; ISUAAAT: Stockholm, Sweden, 2015; p. 14.
24. Philit, M.; Ferrand, P.; Labit, S.; Chassaing, J.C.; Aubert, S.; Fransson, T. Derivated Turbulence Model to Predict Harmonic Loads in Transonic Separated Flows over a Bump. 28th International Congress of the Aeroautical Sciences; ICAS: Brisbane, Australia, 2012; p. 11.
25. Duquesne, P.; Aubert, S.; Rendu, Q.; Ferrand, P. Effect of nodal diameter on the local blades vibration on the choke flutter instability in transonic UHBR fan. 15th International Symposium on Unsteady Aerodynamics, Aeroacoustics and Aeroelasticity of Turbomachines, 2018, p. 10.
26. Brandstetter, C.; Paoletti, B.; Ottavy, X. Compressible Modal Instability Onset in an Aerodynamically Mistuned Transonic Fan. *Journal of Turbomachinery* **2019**, *141*(3): 031004, 13.
27. Allemang, R.J. The Modal Assurance Criterion – Twenty Years of Use and Abuse. *Journal of Sound and Vibration* **2003**, p. 8.
28. Duquesne, P.; Mahieux, B.; Aubert, S.; Ferrand, P. Sensitivity of the aerodynamics damping coefficient prediction to the turbulence modelling conjugated with the vibration mode shape. Proceedings of 13th European Conference on Turbomachinery Fluid dynamics & Thermodynamics ETC13; European Turbomachinery Society: Lausanne, Switzerland, 2019; p. 12.

- 
29. Ferria, H.; Ferrand, P.; Pacull, F.; Aubert, S. Numerical investigation of flutter stability in subsonic space turbine blisk with emphasis on cut-on/cut-off modes and interblade phase angles. *Journal of Thermal Science* **2012**, *21*, 492–499. doi:10.1007/s11630-012-0573-y.
  30. Hellmich, B.; Seume, J.R. Causes of Acoustic Resonance in a High-Speed Axial Compressor. *Journal of Turbomachinery* **2008**, *130*, 031003. doi:10.1115/1.2775487.
  31. Atassi, H.M.; Fang, J.; Ferrand, P. Acoustic blockage effects in unsteady transonic nozzle and cascade flows. 33rd Aerospace Sciences Meeting and Exhibit; AIAA: Reno, Nevada, 1995; Vol. 95-0303, p. 9.